Frequency and Phase Synchronous Control Method Without Communication of the BCPT System

Min Sun, *Graduate Student Member, IEEE*, Xin Dai, *Member, IEEE*, Yugang Su, *Member, IEEE*,
Yanling Li, and Shijun Zhao, *Graduate Student Member, IEEE*

***Abstract*—Bidirectional capacitive power transfer (BCPT) systems provide a flexible and economical method for energy interaction and sharing among multiple electronic devices. BCPT systems utilize two independent controllers for the primary and secondary converters. Out of synchronization between two converters will cause power oscillation and the actual power cannot be guaranteed. This article proposes a synchronous control method of the dual *LCLC*-compensated BCPT system without wireless communication. The method utilizes two pairs of supplementary plates to form the composite plate coupler and then derives a four-port equivalent circuit model from the coupling capacitance model. The induced voltage of secondary supplementary plates is synchronized with the resonant voltage generated by the primary converter so as to obtain the frequency and phase of the primary main plates and feed it back to the secondary controller. Due to the interoperability of the proposed system, the primary supplementary plates can also obtain the synchronization status of the secondary converter and provide feedback to the primary controller. Besides, there is no need for complex data processing analyses of the proposed synchronization control method, which is favorable to operate in a high-frequency BCPT system. The experimental results validate the effectiveness of the proposed synchronous control method in the BCPT systems.**

***Index Terms*—Bidirectional capacitive power transfer (BCPT), eight-plate coupling capacitance model, phase-shift, power flow regulation, synchronous control.**

I. INTRODUCTION

THE capacitive power transfer (CPT) system has attracted extensive attention and research as an alternative to the traditional inductive power transfer system [1]. CPT technology utilizes the electric field as the energy transmission carrier, and the CPT system has special advantages, including light and low cost of coupling structure, low eddy current loss in a metallic conductor and around coupling structures, low electromagnetic interference, and penetrating metal objects without generating significant power losses [2], [3], [4]. The research on the CPT systems has made some achievements in LED lights [5], biomedical equipment [6], bioelectric measurement systems [7], and electric vehicle charging [8], [9]. Meanwhile, more and more scenarios are starting to show the demand for bidirectional wireless power transfer (BWPT) technology, such as vehicles to grid application and shared charging of portable devices, which can help to improve charging convenience, reduce the burden on the grid, and avoid energy waste [10], [11], [12], [13], [14], [15], [16]. Bidirectional capacitive power transfer (BCPT) technology is a kind of BWPT technology, which is considered a potential development tendency [17]. The block diagram of the typical BCPT system is shown in Fig. 1, where V_d represents a dc voltage generated from the single-phase grid through an active rectifier and V_o represents a dc battery voltage. The primary and secondary bidirectional high-frequency converters are used to drive the electric coupling structure and the resonant network.

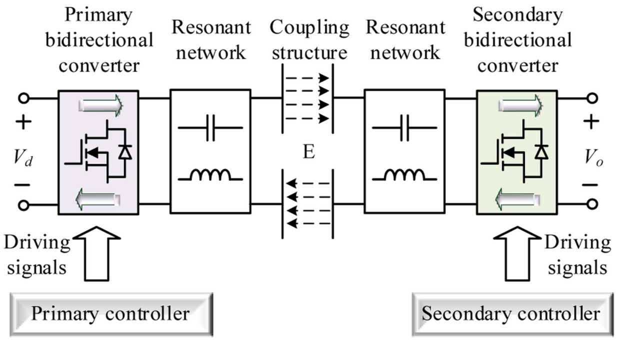

Fig. 1. Block diagram of the typical BCPT system.

The previously proposed BWPT systems usually utilize the identical symmetrical active converter and compensation topology. Typically, the magnitude and direction of power flow are controlled by the relative phase-shift angle or magnitude of the ac voltages produced by the primary and secondary converters [18], [19]. However, the aforementioned bidirectional power flow control strategy is only applicable to the case where the two controllers operate synchronously. Because there is always a frequency difference between the crystal oscillators of two independent controllers on the primary and secondary sides, it will cause the periodic change of the relative phase shift between primary and secondary converters, which will lead to power oscillation [20]. In the traditional BWPT system, synchronization control

---

Manuscript received 16 August 2023; revised 5 November 2023; accepted 2 December 2023. Date of publication 5 December 2023; date of current version 16 February 2024. This work was supported in part by the National Natural Science Foundations of China under Grant 51977178 and in part by China National Center for International Research on Wireless Power Transfer Technology. Recommended for publication by Associate Editor J. Acero. *(Corresponding author: Xin Dai.)*

Min Sun, Xin Dai, Yugang Su, and Shijun Zhao are with the School of Automation, Chongqing University, Chongqing 400044, China (e-mail: sunmin@cqu.edu.cn; daixin@cqu.edu.cn; su7558@qq.com; zsjwpt@cqu.edu.cn).

Yanling Li is with the School of Electrical Engineering and Electronic Information, Xihua University, Chengdu 610039, China (e-mail: yanling.li@mail.xhu.edu.cn).

Color versions of one or more figures in this article are available at https://doi.org/10.1109/TPEL.2023.3339626.

Digital Object Identifier 10.1109/TPEL.2023.3339626

is normally achieved by using wireless communication between the primary- and secondary-side independent controllers [21], [22]. However, due to the high frequency of the BCPT system, commonly used wireless communication techniques, such as Bluetooth, ZigBee, and Wi-Fi, have time delays, making it difficult to achieve the synchronization of the driving signals. Moreover, the wireless communication is sensitive to the cross interference from other communication devices and the electromagnetic interference from the high-frequency electronics' converters [23], [24], [25].

As synchronous control method that avoids the use of wireless communication in the BWPT system is concerned, Liu et al. [26] proposed a synchronous control strategy based on the interference observation method without adding any additional circuits. Apply interference to the relative phase-shift angle: If the power changes in the desired direction, the relative phase-shift angle will continue to increase or decrease in the same direction; otherwise, it will change in the opposite direction. This method can avoid the influence of circuit parameter changes and system detuning, but the power will fluctuate all the time under interference that affects the system stability. In order to reduce the power disturbance and the complexity of the detection circuit, Jia et al. [27] propose a digital phase synchronization control method by detecting the resonant current at the secondary side, considering the current harmonics and the frequency deviation between the controllers of the primary and secondary sides. Zhang et al. [28] proposed a constant current control strategy that periodically synchronizes and corrects the relative phase angle by detecting the secondary resonant current. By detecting the phase of the resonant current at each synchronization cycle to adjust the phase shift of the secondary converter, the relative phase angle is kept stable to achieve constant power transfer. However, the current detection synchronous control method may result in synchronization failure due to the possible harmonics current. Tang et al. [29] proposed a controller that implemented the zero reactive power control for the bidirectional inductive power transfer (BIPT) system by detecting the resonance voltage and current of the secondary side and using the analog circuit to calculate the active and reactive power. Although the control method can still achieve synchronization while adapting to the variation of system parameters, however, the proposed control method requires complex analog signal processing circuits, including an analog multiplier, analog phase shifter, and low-pass filter, which has a delay in high-frequency system and reduces the control performance. In addition, both the synchronization control strategy of ensuring zero reactive power and the bidirectional power flow regulation adopt the phase-shift angle regulation, which may cause mutual coupling interference, especially in the high-frequency system. Thrimawithana et al. [30] proposed a synchronization technique of the BIPT system that employed a sense winding wound on the pickup inductor to derive a voltage signal by sensing the magnetic field generated by the primary resonant current, which is synchronization with the voltage vector produced by the primary converter. However, the synchronization voltage sensed by the sense winding affected by the magnetic field of the pickup is negated by the sensing voltage from the compensation winding of the pickup toroidal ferrite core. And the synchronization technique adopts a phase-locked loop (PLL) with the voltage-controlled oscillator (VCO) to feed the synchronization signal to the controller.

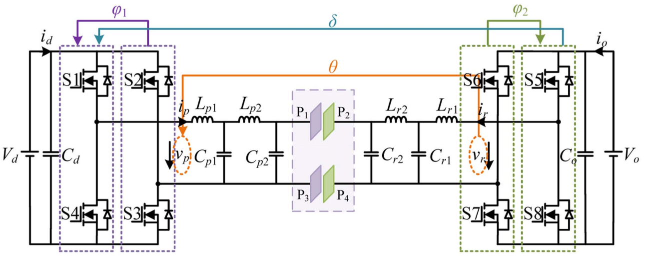

Fig. 2. Circuit diagram of the dual *LCLC*-compensated topology BCPT system.

The pieces of literature mentioned above on the synchronous control method are for the BIPT system, and there are few publications on the synchronization control for the BCPT systems. Therefore, in order to achieve synchronization between the primary and secondary sides of the BCPT system under high-frequency operation, without any bilateral communication modules, this article proposes a frequency and phase synchronization control method for the dual *LCLC*-compensated BCPT systems by adding two pairs of supplementary plates. Compared with [30], the proposed synchronous control method allows for the identification of the synchronization status of the primary side to the secondary side by detecting the terminal voltage of the secondary supplementary plates, which is not affected by the output voltage of the secondary converter. And the synchronization status of the secondary side can also be identified to the primary controller through the terminal voltage of the primary supplementary plates, achieving synchronization and interoperability between the primary and secondary controllers. Besides, the proposed synchronous control method does not require PLL, VCO, complex analog circuits, and data processing analyses, which is favorable to operation at high frequency and accurate power flow regulation of the BCPT system. The experimental result of the BCPT system is presented to show that the proposed synchronous control method is feasible and applicable.

II. TOPOLOGY AND MODELING OF THE BCPT SYSTEM

The dual *LCLC*-compensated topology has the advantage, such as the transmission power is proportional to the coupling coefficient of the coupling plates, providing good performance in case of coupling misalignment and parameter variation, and also reducing the current and voltage stress of the circuit components near the coupling plates [31], [32]. This article adopts the dual *LCLC*-compensated topologies of the BCPT system, as shown in Fig. 2, to realize the energy interaction between the grid and battery-equipped devices conveniently, where L_{p1}, L_{p2}, L_{r1}, and L_{r2} are the self-inductances of the coils, C_{p1}, C_{p2}, C_{r1}, and C_{r2} are the compensated capacitances, and C_d and C_o are the dc filter capacitors. V_d is the dc-link voltage and is usually kept constant from the grid-connected ac–dc active rectifier, and V_o is the dc voltage of the battery. i_d and i_o are the primary and secondary dc

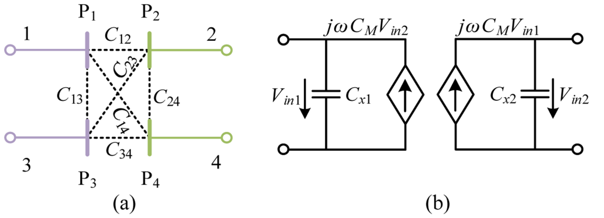

Fig. 3. Circuit model of capacitive coupler. (a) Four-plate capacitor model. (b) Equivalent two-port model.

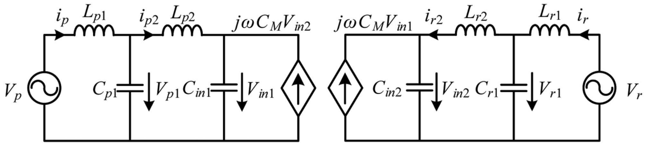

Fig. 4. Simplified circuit of an equivalent current-source model.

input currents. v_p and v_r are the ac resonant voltages generated by the primary and secondary full-bridge converters, and i_p and i_r are the primary- and secondary-side ac resonant currents. Power will be wirelessly transferred between the plates under the action of the interactive electric field. The primary and secondary circuits are implemented with virtually identical electronics to facilitate bidirectional power flow.

The capacitive coupler contains four metal plates P_1–P_4. P_1 and P_3 are placed on the primary side, while P_2 and P_4 are placed on the secondary side. There are capacitive couplings between every two plates, which result in six capacitors C_{12}–C_{34}, as shown in Fig. 3. It is further simplified as a two-port model in which C_{x1} and C_{x2} are the internal self-capacitances and C_M is the equivalent mutual capacitance. Fig. 4 shows the simplified circuit diagram of BCPT system with an equivalent current-source model. The equivalent current source related to the capacitor voltage represents the capacitance coupling between the primary- and secondary-side plates. The equivalent self-capacitance and coupling coefficient can be expressed as follows:

$$\begin{aligned} &C_{\text{in}1} = C_{p2} + C_{x1}, \quad C_{\text{in}2} = C_{r2} + C_{x2} \\ &k_c = C_M \Big/ \sqrt{C_{\text{in}1} \cdot C_{\text{in}2}} \end{aligned} \tag{1}$$

where

$$\begin{aligned} C_{x1} &= C_{13} + \frac{(C_{12} + C_{14})(C_{23} + C_{34})}{C_{12} + C_{14} + C_{23} + C_{34}} \\ C_{x2} &= C_{24} + \frac{(C_{12} + C_{23})(C_{14} + C_{34})}{C_{12} + C_{14} + C_{23} + C_{34}} \\ C_M &= \frac{C_{12}C_{34} - C_{14}C_{23}}{C_{12} + C_{14} + C_{23} + C_{34}}. \end{aligned} \tag{2}$$

The primary and secondary compensation networks are usually designed to resonate at the switching frequency of f_s, and

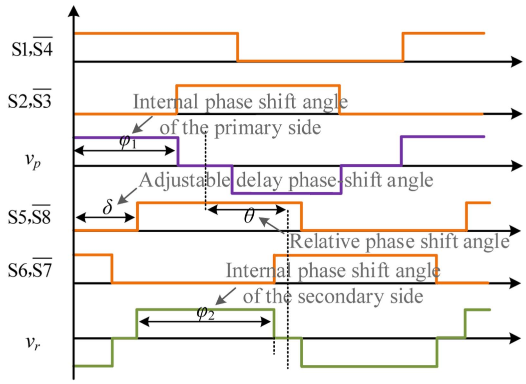

Fig. 5. Driving signals and resonant voltage waveforms of the primary- and secondary-side converters.

then

$$\begin{cases} \omega^2 L_{p2}\left(C_{p1} \cdot C_{\text{in}1} / \left(C_{p1} + C_{\text{in}1}\right)\right) = 1 \\ \omega^2 C_{p1}\left(L_{p1} \cdot L_{p2} / \left(L_{p1} + L_{p2}\right)\right) = 1 \\ \omega^2 L_{r2}\left(C_{r1} \cdot C_{\text{in}2} / \left(C_{r1} + C_{\text{in}2}\right)\right) = 1 \\ \omega^2 C_{r1}\left(L_{r1} \cdot L_{r2} / \left(L_{r1} + L_{r2}\right)\right) = 1 \end{cases} \tag{3}$$

where $\omega = 2\pi f_s$.

As shown in Fig. 2, all switches ($S1$–$S4$ and $S5$–$S8$) of the primary and secondary converters are operated with a 50% duty cycle and at switching frequency to produce v_p and v_r, with the internal phase-shift angles φ_1 and φ_2 between the two legs of each converter. As shown in Fig. 5, δ is the adjustable delay phase-shift angle between the switches $S1$($S4$) and $S5$($S8$). θ is the relative phase-shift angle of the primary and secondary resonant voltage. In order to obtain a mathematical model for the power throughput of the proposed BCPT system, the fundamental voltages of v_p and v_r are given by

$$\begin{aligned} v_p &= \frac{4}{\pi} V_d \cos(\omega t) \sin\left(\frac{\varphi_1}{2}\right) \\ v_r &= \frac{4}{\pi} V_o \cos(\omega t - \theta) \sin\left(\frac{\varphi_2}{2}\right). \end{aligned} \tag{4}$$

By adopting the first harmonic approximation method and ignoring the internal resistance loss, according to KVLs law, the relationship between the currents and voltages of the BCPT system, as shown in Fig. 4, can be derived as

$$\begin{cases} V_p = j\omega L_{p1} I_p + V_{p1} \\ I_p = j\omega C_{p1} V_{p1} + I_{p2} \\ V_{p1} = j\omega L_{p2} I_{p2} + V_{\text{in}1} \\ I_{p2} = j\omega C_{\text{in}1} V_{\text{in}1} - j\omega C_M V_{\text{in}2} \\ I_{r2} = j\omega C_{\text{in}2} V_{\text{in}2} - j\omega C_M V_{\text{in}1} \\ V_{\text{in}2} = V_{r1} - j\omega L_{r2} I_{r2} \\ I_r = j\omega C_{r1} V_{r1} + I_{r2}. \end{cases} \tag{5}$$

Under the condition of (4), the voltage of $V_{\text{in}1}$ across the capacitor $C_{\text{in}1}$ can be expressed by

$$V_{\text{in}1} = -\frac{L_{p2}}{L_{p1}} V_p. \tag{6}$$

The resonant current of the secondary side can be derived as

$$I_r = j\omega C_M \frac{L_{r2}}{L_{r1}} V_{\text{in1}} = -j\omega C_M \frac{L_{p2}L_{r2}}{L_{p1}L_{r1}} V_p. \tag{7}$$

From (7), it can be seen that the secondary resonant current only depends on the primary resonant voltage under the given circuit parameters of the proposed BCPT system. Thus, the transmission power of the secondary side can be given by

$$P_r = \mathrm{Re}\left\{V_r I_r^*\right\} = \frac{8\omega C_M}{\pi^2}\frac{L_{p2}L_{r2}}{L_{p1}L_{r1}} V_d V_o \sin\theta \sin\frac{\varphi_1}{2} \sin\frac{\varphi_2}{2} \tag{8}$$

where $0 < \varphi_1 \ll \pi$ and $0 < \varphi_2 \ll \pi$, as illustrated in Fig. 5.

Therefore, under the given circuit parameters and dc voltage, it is obvious from (8) that the magnitude of transmission power can be regulated by either controlling φ_1 and φ_2 of the voltages generated by the converters or modulating θ, the direction of power flow only depends on θ. Additionally, θ can be modulated for any combination of δ, $\varphi 1$, and $\varphi 2$. When $0° < \theta < 180°$ and $P_r > 0$, a lagging phase angle enables power transfer from the secondary to the primary side; while when $-180° < \theta < 0°$ and $P_r < 0$, a leading phase angle constitutes power transfer from the primary to the secondary side. Besides, the maximum transmission power takes place when θ is $\pm 90°$.

III. Proposed Synchronous Control Method

From (8), it is noted that the system power flow can be regulated by the relative phase-shift angle between v_p and v_r of the proposed BCPT system with the dual *LCLC*-compensated network. However, in the phase-shift power flow regulation process of the BCPT system, the primary and secondary sides need to rely on the synchronous driving signal of two independent controllers to achieve synchronization between the converters of the primary and secondary sides and satisfy the actual power flow transmission. Otherwise, it will lead to the deviation of the direction and magnitude of the power flow, and the system transmission power in any direction cannot be guaranteed. Therefore, synchronous control has a vital impact on the power regulation of the BCPT system.

In order to realize the synchronization of the proposed BCPT system and the interoperability of the primary and secondary independent controllers, two pairs of supplementary plates (P_p, P_q, P_r, and P_s) are added to the two pairs of main plates (P_1, P_2, P_3, and P_4). The structure of the eight-plate coupler is shown in Fig. 6. The specific design dimensions and parameters are shown in Table I. P_1 and P_3, and P_2 and P_4 are the main plates connecting the primary and secondary circuits. P_p and P_q, and P_r and P_s are the supplementary plates of the primary and secondary circuits, respectively. The eight-plate coupler is composed of two printed circuit boards (PCB). PCB1 is fabricated by the 1.5-mm-thick FR-4 dielectric layer and the copper plates P_1, P_r, P_3, and P_s. PCB2 is fabricated by the 1.5-mm-thick FR-4 dielectric layer and the copper plates P_2, P_p, P_4, and P_q.

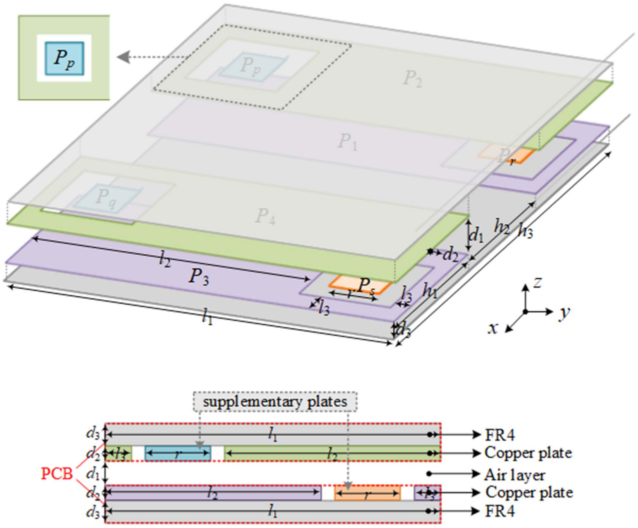

Fig. 6. Structure of an eight-plate coupler.

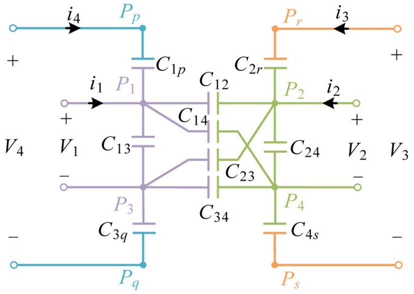

Fig. 7. Simplified coupling capacitance model of an eight-plate coupler.

In the eight-plate coupler, there are coupling capacitances between each two plates. Since the size of the supplementary plates is designed to be relatively small, and the distance between the main plates and vertical contralateral supplementary plates is close, the cross coupling between the supplementary plates and other plates (such as C_{1r}, C_{1q}, and C_{1s}) is weak, and the coupling capacitances are less than 1 pF. According to the weight analytic method, they are neglected. Thus, only the coupling capacitances (C_{1p}, C_{2r}, C_{3q}, and C_{4s}) between the supplementary plates and the main plates vertically coupled are considered, while some of the cross-coupling capacitances are ignored. The simplified coupling capacitance model is shown in Fig. 7, where V_1 and V_2 are the plates' voltages at the primary and secondary sides, respectively. V_3 and V_4, and I_3 and I_4 are the imaginary external excitations between the supplementary plates P_r and P_s and P_p and P_q.

Therefore, according to the simplified coupling capacitance model, the four-port equivalent circuit diagram with an eight-plate coupler structure of the proposed BCPT system is obtained, as shown in Fig. 8; all the capacitance values of coupling plates are listed in Table II. The specific derivation process is provided in the Appendix. V_3 and V_4 are the sensed terminal voltages by the supplementary plates that can be expressed as

$$\begin{cases} V_3 = \frac{j\omega C_{M3}}{j\omega C_3} V_2 = -\frac{L_{r2}}{L_{r1}} V_r \\ V_4 = \frac{j\omega C_{M2}}{j\omega C_4} V_1 = -\frac{L_{p2}}{L_{p1}} V_p \end{cases} \tag{9}$$

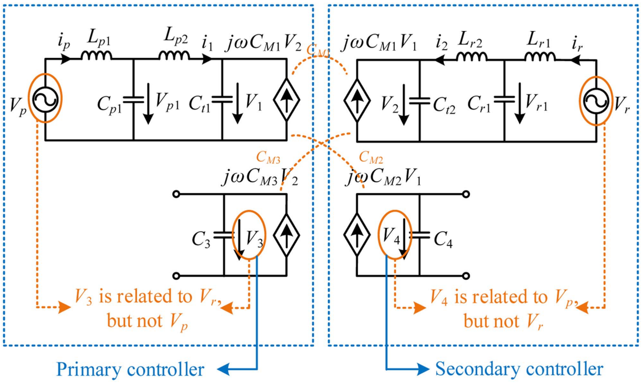

Fig. 8. Four-port equivalent circuit diagram with an eight-plate coupler structure of the proposed BCPT system.

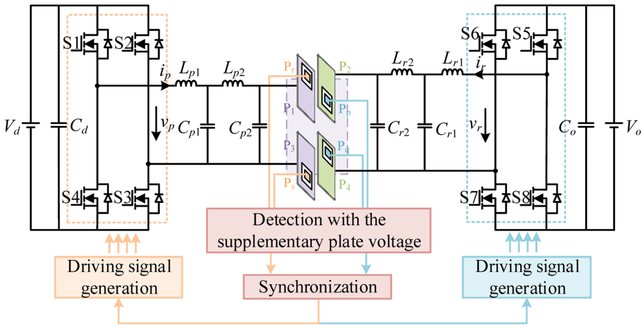

Fig. 9. Block diagram of the proposed control strategy.

where the mutual capacitance C_{M2} (C_{M3}) can be expressed as

$$\begin{cases} C_{M2} = \frac{C_{1p}C_{3q}}{C_{1p}+C_{3q}} \\ C_{M3} = \frac{C_{2r}C_{4s}}{C_{2r}+C_{4s}}. \end{cases} \tag{10}$$

From (9), it can be seen that the synchronization signal V_4 (V_3) is the explicit expression of V_1 (V_2) under the given circuit parameters, which is synchronized with the resonant voltage V_p (V_r) generated by the primary (secondary) converter. Therefore, the terminal voltage of V_4 at the secondary supplementary plates P_p and P_q is only related to the resonant voltage V_p of the primary converter and has a phase difference of 180°, and is independent of the resonant voltage V_r of the secondary converter. Similarly, the terminal voltage of V_3 at the primary supplementary plates P_r and P_s is only related to V_r and has a phase difference of 180°, not V_p.

Therefore, two pairs of the supplementary plates are designed on the main plates to induce the electric field generated by the main plates, as shown in Fig. 9, so as to obtain the induced voltage signal on the supplementary plates, which is synchronized with the resonant voltage generated by the converter. Then, the primary(secondary) controller obtains the phase and frequency information of the secondary(primary) main plates from the primary(secondary) supplementary plates so as to achieve the interaction and interoperability between the primary and secondary sides for bidirectional wireless charging devices.

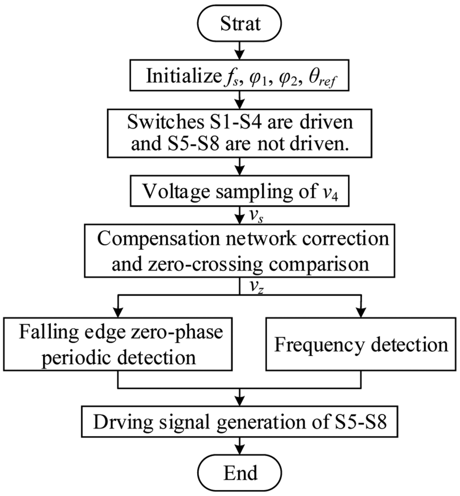

Fig. 10. Flowchart of synchronization control technology.

Take the acquisition of the terminal voltage v_4 of the secondary supplementary plate as an example, the secondary controller obtains the synchronization information of primary side from the secondary supplementary plates to illustrate the frequency and phase synchronization of the BCPT system. The flowchart of the proposed control method is shown in Fig. 10.

1) Initialize the values of f_s, φ_1, φ_2, and θ_{ref}, where f_s is the resonant frequency driving the primary converter, φ_1 is determined by the expected resonant voltage of v_p, φ_2 is preset to 180°, θ_{ref} is determined by the expected power transmission direction, and during the synchronization process, θ_{ref} is preset as $-90°$ when the system is expected to be in forward power transmission, while θ_{ref} is preset as 90° when is expected to be in reverse power transmission.
2) The switches $S1$–$S4$ of the primary converter are driven and operate as an inverter, while the switches $S5$–$S8$ of the secondary converter are not driven and operate as a rectifier.
3) The terminal voltage v_4 of the secondary supplementary plates is passed through a differential amplifier to obtain the sampling voltage of v_s.
4) v_s is passed through the compensation network and fed to the zero-crossing comparator to obtain the synchronous signal of v_z.
5) When the falling edge of v_z is triggered, the secondary controller counts with a value of "Count" to obtain the operating frequency.
6) The falling edge of v_z is detected to drive signal generation for the switches $S5$–$S8$ of the secondary converter according to the obtained operating frequencies θ_{ref} and φ_2.
7) Repeatedly detect the falling edge of v_z at intervals and regenerate driving $S5$–$S8$ to correct the phase deviation between the counter and v_z.

Through the above process of the proposed synchronous control method, the secondary controller obtains the operating frequency of the primary converter and the relative phase-shift

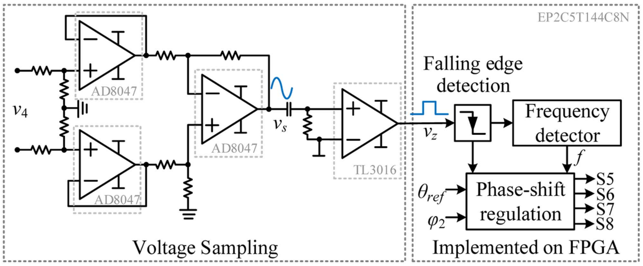

Fig. 11. Schematic diagram of the proposed synchronization control method.

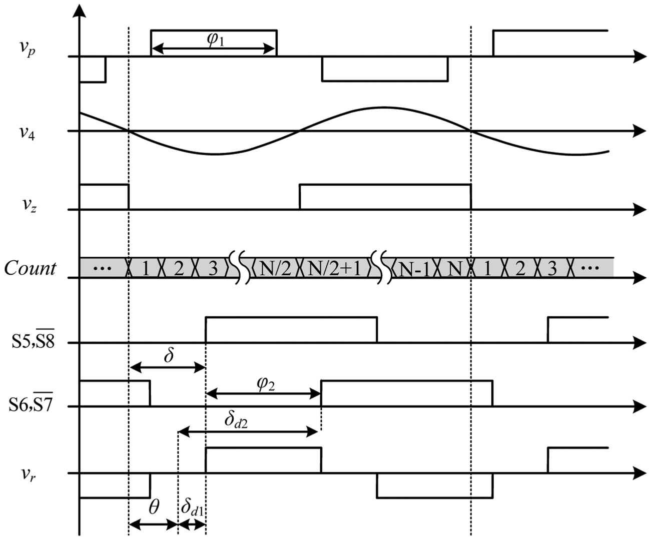

Fig. 12. Sequences of synchronization control technology.

angle is fixed at θ_{ref} between the resonant voltage of the primary and secondary sides, thereby achieving the frequency and phase synchronization between the primary and secondary sides.

The schematic diagram and specific sequences of synchronization control technology are shown in Figs. 11 and 12. At first, the terminal voltage of v_4 generated by the supplementary plates is passed through the operational amplifier to obtain the sampling voltage of v_s and phase corrected for the time delay by the *RC* compensation network, which is then fed to the zero-crossing comparator. By feeding the signal of v_z to the field-programmable gate array (FPGA) and v_z is antiphase with the resonant voltage v_p of the primary converter, FPGA captures and cycle counts the falling edge of v_z and starts counting when the first falling edge of v_z is triggered, ends counting when the second falling edge is triggered. The pulse counter writes the number of pulses into the counting register to obtain the operating frequency of v_z. Thus, the secondary controller generates a synchronous counter synchronized with the falling edge of v_z, and the value in the counter is used to derive the operating frequency of the primary controller to the secondary controller. "Count" is the number of counts per cycle of the falling edge of v_z by the counter. At the same time, the high level of the counter edge is in phase with v_z. According to the frequency generated by the synchronous counter, the expected relative phase-shift angle θ_{ref} can be generated through phase-shifting regulation of the switches *S*5–*S*8 of the secondary-side converter. Phase-shifting regulation has two inputs with θ_{ref} and φ_2. *S*5 and *S*8 are the phase shifts regulated by θ_{ref} and δ_{d1}, and *S*6 and *S*7 are the phase shifts regulated through θ_{ref} and δ_{d2}, where $\delta_{d1} = (\pi - \varphi_2)/2$ controls the phase shift between v_r and the switches of *S*5 and *S*8, and $\delta_{d2} = (\pi + \varphi_2)/2$ controls the phase shift between v_r and the switches of *S*6 and *S*7.

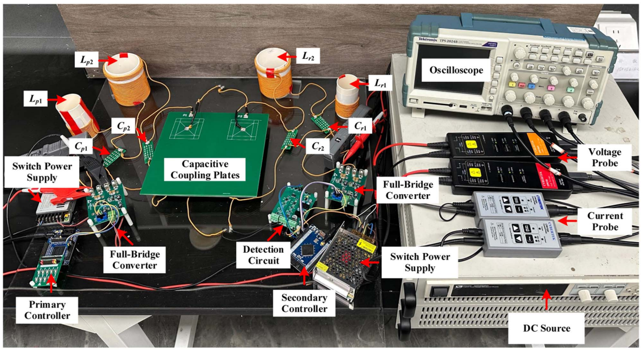

Fig. 13. Schematic diagram of the experimental setup.

After frequency and phase synchronization between the primary and secondary sides of the proposed system, according to the internal phase-shift angle φ_1 of the primary converter, the desired power of P_{ref} and (29), power magnitude, and direction regulation can be achieved by adjusting θ or φ_2, which can be generated by the switches of the secondary-side converter, where *S*5 and *S*8 are phase shifted by θ and δ_{d1}, and *S*6 and *S*7 are phase-shifted by θ and δ_{d2}, where $\delta_{d1} = (\pi - \varphi_2)/2$ and $\delta_{d2} = (\pi + \varphi_2)/2$.

In order to ensure accurate detection of the frequency and phase with voltage sampling process of the high-frequency BCPT system, several aspects are worth to be noted as follows.

1) When selecting a high-speed operational amplifier, it is necessary to focus on factors, such as bandwidth gain and slew rate. The operational amplifier with high gain and sufficient bandwidth can usually be selected and retained with a certain margin. Moreover, the wider the bandwidth, the faster the response speed, which can reduce the detection error caused by high-frequency signals.
2) Zero-crossing comparator needs to have high-speed response capability to ensure the low latency and accuracy of voltage sampling.
3) A compensation network is required for delays caused by the voltage detection, zero-crossing comparison, and FPGA operation.

IV. EXPERIMENTAL RESULTS

Following the analysis made in Section III, the synchronization control method by detecting the voltage of the supplementary plates is proposed in the BCPT system accordingly. A BCPT prototype with the proposed synchronization method is constructed to validate the effectiveness of the control technique, as shown in Fig. 13. The system comprises primary and

TABLE I
PARAMETERS OF THE EIGHT-PLATE COUPLER

Parameter	Value	Parameter	Value
l_1 (mm)	220	l_2(mm)	140
l_3(mm)	20	h_1(mm)	100
h_2(mm)	20	h_3(mm)	220
d_1(mm)	1	d_2(mm)	0.036
d_3(mm)	1.6	r(mm)	40

secondary full-bridge converters, which were controlled by two independent microcontrollers. The converters are realized with GaN power modules.

The capacitive coupler structure is designed with structures and dimensions, as presented in Fig. 6 and Table I, and two PCBs were fabricated to integrate the capacitive coupler. The circuit parameters of the experimental prototype are designed symmetric from primary to secondary side and summarized, as listed in Table III. The parallel resonant capacitors C_{p1}, C_{p2}, C_{r1}, and C_{r2} use high-voltage multilayer surface-mounted device ceramic capacitors. The compensation inductors L_{p1}, L_{p2}, L_{r1}, and L_{r2} are made of Litz-wire wound on polyvinyl chloride tubes, which are selected according to the resonance relationships in (25) at the resonant frequency of 1 MHz.

The terminal voltage of the supplementary plates is sampled by the operational amplifier (AD8057) and the high-speed zero-crossing comparator (TL3016). Then, the falling edge detection and counting of the synchronous voltage signal are performed by FPGA (EP2C5T144C8N) to achieve frequency and phase synchronization of the proposed system.

Considering that the input voltage of the operational amplifier cannot exceed its supply voltage, and the terminal voltage V_4 of the supplementary plates is about 200 V in the proposed system, a 200:1 resistor voltage divider network is set at the input of the voltage detection circuit.

Fig. 14(c) shows the experimental results of the frequency and phase synchronization control transient behavior of the BCPT system, including the output voltage v_p of the primary converter, the voltage v_1 of the primary main plates, the synchronization signal v_4, and the switch driving signal *S5* of the secondary converter. As evident from the results, initially, the primary converter is turned ON with f_s and operates in the inverter mode by the primary controller; the secondary converter operates in the uncontrolled-rectifier mode. The steady-state waveform of the proposed system at $\varphi_1 = 180°$ is shown in Fig. 14(a), and a 700 V and 1 MHz sinusoidal voltage v_1 is generated on the primary main plates. The proposed system detects the terminal voltage v_4 of the secondary supplementary plates, which is in synchronization with v_1. As predicted in (9), the synchronous signal v_4 generated by the proposed system is antiphase with v_p. The secondary controller generates a counter synchronized with v_p by the sampling and falling edge detecting the synchronous signal v_4. At the moment of t_1, a square-wave signal synchronized with v_p is used to drive the secondary converter to generate a relative phase difference of 90° ($\theta_{\mathrm{ref}} = 90°$ and $\varphi_2 = 180°$), as shown in Fig. 14(b), v_r lagging v_p by 90°, and v_r and i_r is in phase, which indicates that the primary side receives the power transferred from the secondary. When $t > t_1$, the falling edge of v_z is repeatedly detected at intervals and regenerates driving *S5*–*S8* to correct the phase deviation between the counter and v_z. The enlarged transient waveforms within 50 μs are shown in Fig. 14(d); it can be seen from the initial stage of 241.1 μs and the final stage of 287.5 μs, as shown in Fig. 14(e) and (f), that the relative phase-shift angle of θ_{ref} is no change within a duration of 46.4 μs, which is about 46 operating cycles. Therefore, θ_{ref} is fixed at the expected relative phase-shift angle and the proposed system achieves synchronization of the primary- and secondary-side frequency and phase.

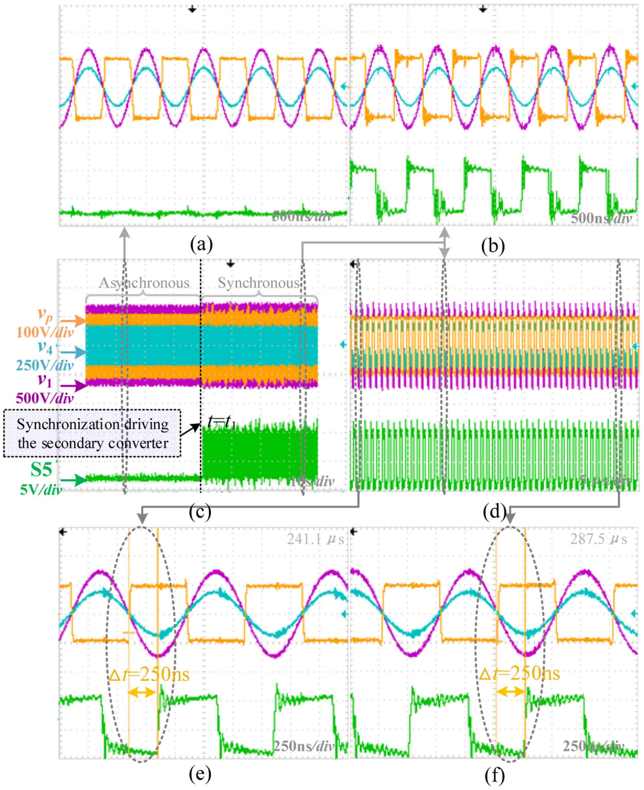

Fig. 14. Experimental results of synchronous control transient response at $\varphi_1 = 180°$, $\theta_{\mathrm{ref}} = 90°$, and $\varphi_2 = 180°$. (a) Zoomed-in view of (c) with the asynchronous steady state. (b) Zoomed-in view of (c) with the synchronous steady-state. (c) Full view of the envelopes of v_p, v_4, v_1, and *S5*. (d) Transient response of synchronous control within 50 μs. (e) Zoomed-in view with the initial stage from 241.1 μs of (d). (f) Zoomed-in view with the final stage from 287.5 μs of (d).

From the experimental waveforms of the frequency and phase synchronous control, it is evident that the turn-ON of the secondary converter does not affect the synchronous signal. This is mainly due to the insignificant coupling between the synchronous voltage signal of v_4 and the resonant voltage v_r of the secondary converter, as shown in the mathematical analysis of Section III.

When v_p has a phase-shift angle of $\varphi_1 = 120°$, the experimental results of transient synchronization response are performed, as shown in Fig. 15. Similar to Fig. 14, after sampling and falling edge detecting v_4, when $t = t_1$, the secondary converter is driven

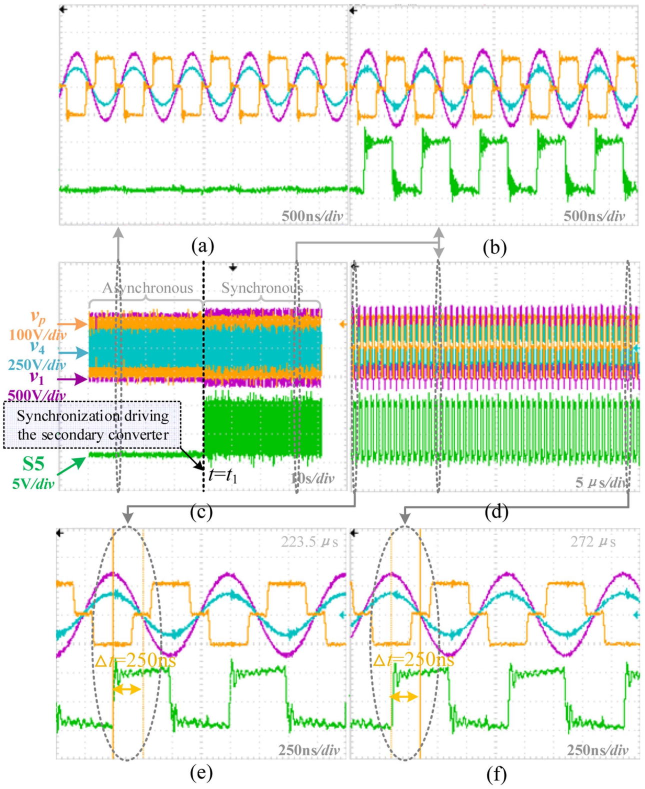

Fig. 15. Experimental results of synchronous control transient response at $\varphi_1 = 120°$, $\theta_{\mathrm{ref}} = -90°$, and $\varphi_2 = 180°$. (a) Zoomed-in view of (c) with the asynchronous steady state. (b) Zoomed-in view of (c) with the synchronous steady state. (c) Full view of the envelopes of v_p, v_4, v_1, and *S5*. (d) Transient response of synchronous control within 50 μs. (e) Zoomed-in view with the initial stage from 223.5 μs of (d). (f) Zoomed-in view with the final stage from 272 μs of (d).

by a square-wave signal synchronized with v_p under $\theta_{\mathrm{ref}} = -90°$ and $\varphi_2 = 180°$, and v_r leading v_p by 90°, indicating the forward power transmission of the proposed system. Fig. 15(c) shows the synchronization control transient behavior, while the uncontrolled and asynchronous waveforms are shown in Fig. 15(a) and the synchronous state is shown in Fig. 15(b). In addition, the enlarged transient waveforms within 50 μs are shown in Fig. 15(d); it can be seen from 223.5 and 272 μs, as shown in Fig. 15(e) and (f), that θ_{ref} of $-90°$ has no change within a duration of 48.5 μs, which is about 48 operating cycles, which indicates that θ_{ref} is fixed at the expected relative phase-shift angle and the proposed system achieving the synchronization of the primary and secondary sides frequency and phase.

When the proposed BCPT system achieves the frequency and phase synchronization, the resonant voltage of the secondary converter is varied by adjusting φ_2 by continuously detecting the zero phase of the falling edge of v_z to regulate the magnitude of power. According to (29), the proposed system is operating in the reverse transmission direction at $\theta = 90°$. Fig. 16(a) shows the transient waveforms of the primary and secondary resonant voltages and currents when the proposed system adjusts φ_2 to regulate the output power at $\varphi_1 = 180°$. In detail, Fig. 16(c) and (d) shows the enlarged resonant voltage and current waveforms

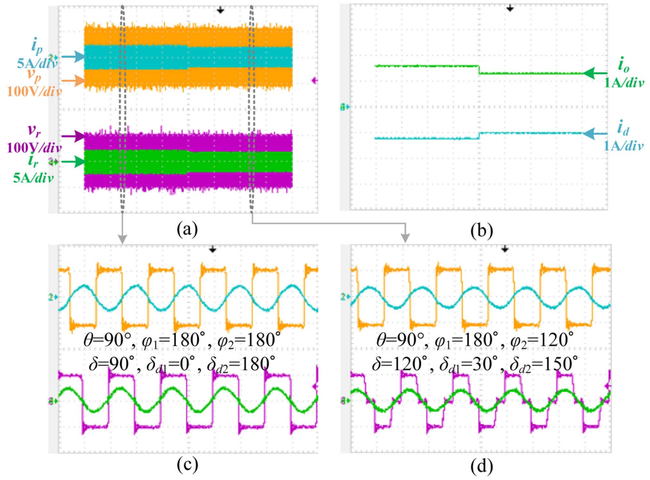

Fig. 16. Experimental results when changing power from 120 to 100 W when the secondary side delivers power to the primary side. (a) Full view of the envelopes of v_p and i_p, and v_r and i_r. (b) DC output currents of i_d and i_o. (c) Zoomed-in view with the initial stage of (a). (d) Zoomed-in view with the final stage of (a).

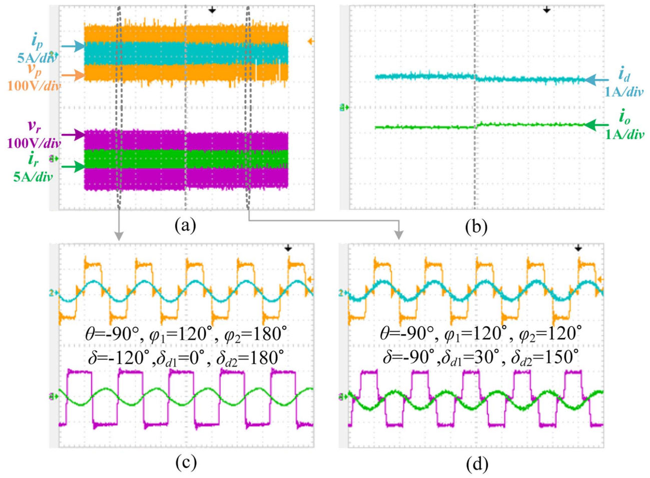

Fig. 17. Experimental results when changing power from 80 to 70 W when the primary side delivers power to the secondary side. (a) Full view of the envelopes of v_p and i_p, and v_r and i_r. (b) DC output currents of i_d and i_o. (c) Zoomed-in view with the initial stage of (a). (d) Zoomed-in view with the final stage of (a).

when φ_2 is changed from 180° to 120°, respectively, where δ_{d1} is varied from 0° to 30°, and δ_{d2} is varied from 180° to 150°. Fig. 16(b) shows the dc current waveforms of i_d and i_o when delivering approximately from 120 to 100 W to the secondary side.

Similar to Fig. 16, when v_p is preset as a phase-shift voltage at $\varphi_1 = 120°$, the system operating in the forward power transmission direction at $\theta = -90°$ is shown in Fig. 17, and φ_2 is changed from 180° to 120°, where δ_{d1} is varied from 0° to 30°, and δ_{d2} is varied from 180° to 150°. Fig. 17(a) shows the experimental results of the power regulation transient behavior of the BCPT system, including the output waveforms of the resonant voltages v_p and v_r and resonant currents i_p and i_r of the primary and secondary converters. It can be seen from the

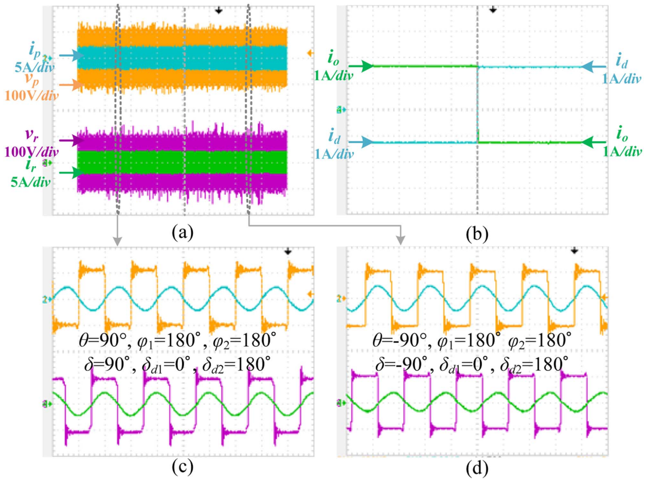

(a) (b) (c) (d)

Fig. 18. Experimental results when changing the direction of power flow. (a) Full view of the envelopes of v_p and i_1, and v_r and i_2. (b) DC output currents of i_d and i_o. (c) Zoomed-in view with the initial stage of (a). (d) Zoomed-in view with the final stage of (a).

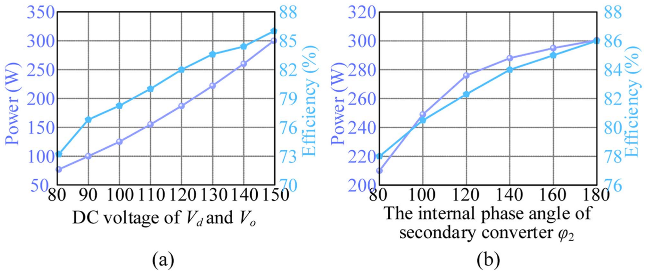

(a) (b)

Fig. 19. Transmission power and efficiency. (a) Varies with V_d and V_o. (b) Varies with φ_2.

variation waveforms of dc currents i_d and i_o in Fig. 17(b) that the system forward power transmission varies from about 80 to 70 W. Specifically, as evident from Fig. 17(c), Fig. 17(d) shows the enlarged resonant voltage and current waveforms, respectively.

Fig. 18(a) shows the transient resonant voltage and current waveforms when the system changes the direction of the power flow by changing the relative phase-shift angle θ from 90° to $-90°$. It can be depicted from Fig. 18(b) that the system transmission power is about 120 W when operating in the reverse transmission direction. After a period of time, the system operates in forward transmission. Specifically, Fig. 18(c) and (d) shows the enlarged resonant voltage and current waveforms, respectively. The voltage and current magnitudes of both converters are similarly corresponding to the forward and reverse power flow. Therefore, it should be noted that the proposed BCPT system can reverse the direction of power flow between the primary- and secondary-side converters without interrupting the operation of the converters.

Due to the symmetry structure of the proposed system, the power and efficiency curves of forward and reverse transmission are almost identical. When the primary controller provided the driving signal with full pulsewidth for the primary converter and the relative phase-shift angle of θ is $-90°$, Fig. 19 shows the forward transmission power and dc–dc efficiency varies with the dc voltage and the internal phase-shift angle φ_2 of the secondary converter. The transmission power and efficiency vary with dc voltage from 80 to 150 V, as shown in Fig. 19(a); it can be seen that power and efficiency increase with the increase of dc voltage. While Fig. 19(b) shows the power and efficiency vary with φ_2 from 180° to 80°, it can be shown that the power and efficiency decrease with the decrease of φ_2. And the efficiency reaches 86% when the transmission power is 300 W.

V. DISCUSSION

Due to the high operating frequency of the proposed system, the resonance condition of (25) will be deviated inevitably. Suppose that the ratio of driving frequency f_s and resonance frequency f_c is a, it can be expressed as

$$a = \frac{f_s}{f_c}. \tag{11}$$

The resonance relationship can be modified as follows:

$$\begin{cases} \omega_s^2 L_{p2}\left(C_{p1}\cdot C_{t1}/(C_{p1}+C_{t1})\right) = a^2 \\ \omega_s^2 C_{p1}\left(L_{p1}\cdot L_{p2}/(L_{p1}+L_{p2})\right) = a^2 \\ \omega_s^2 L_{r2}\left(C_{r1}\cdot C_{t2}/(C_{r1}+C_{t2})\right) = a^2 \\ \omega_s^2 C_{r1}\left(L_{r1}\cdot L_{r2}/(L_{r1}+L_{r2})\right) = a^2. \end{cases} \tag{12}$$

Thus, from (26), V_3 and V_4 can be given as

$$\begin{cases} V_3 = \frac{1-(1+g)a^2-(1+g)^2\left(1-a^2\right)a^2}{F} V_r \\ \quad + \frac{-\omega_s^2 C_{M1} L_{p2}(1+g)^2\left(1-a^2\right)}{F} V_p \\ V_4 = \frac{1-(1+g)a^2-(1+g)^2\left(1-a^2\right)a^2}{F} V_p \\ \quad + \frac{-\omega_s^2 C_{M1} L_{p2}(1+g)^2\left(1-a^2\right)}{F} V_r \end{cases} \tag{13}$$

where

$$\begin{cases} g = \frac{L_{p1}}{L_{p2}} = \frac{C_{t1}}{C_{p1}} \\ F = \left(1-(1+g)a^2-(1+g)^2\left(1-a^2\right)a^2\right)^2 \\ \quad -\omega_s^2 C_{M1}^2(1+g)^3\left(1-a^2\right)^2 a^2. \end{cases} \tag{14}$$

Thus, the phase angle of γ between V_3 and V_r (V_4 and V_p) can be given as

$$\gamma = f(a, \theta). \tag{15}$$

Therefore, according to the circuit parameters of the proposed system in Tables II and III, the variation of the synchronous phase angle γ with the deviation resonance frequency under different relative phase-shift angles is shown in Fig. 20.

It can be seen from Fig. 20 that γ is fixed at 180° and independent of θ under the resonance condition (i.e., $a = 1$). Thus, the synchronization signal V_4 (V_3) is synchronized with the resonant voltage V_p (V_r) generated by the primary (secondary) converter and is independent of the resonant voltage V_r of the secondary converter. The proposed control method with frequency and phase synchronization of the primary and secondary sides can be achieved by sampling and detecting the falling edge of V_3 or V_4. However, γ varies slightly when the resonance frequency deviates. For example, when $a = 1.01$ with a 1% deviation of the resonance frequency: While $\theta = 90°$, the phase angle deviation

TABLE II
CAPACITANCE VALUES OF COUPLING PLATES

Parameter	Value	Parameter	Value
C_{12} (pF)	157.7	C_{34}(pF)	158.6
C_{13}(pF)	1.8	C_{24}(pF)	1.8
C_{14}(pF)	1.1	C_{23}(pF)	1.2
C_{1p}(pF)	16.7	C_{3q}(pF)	16.7
C_{2r}(pF)	16.6	C_{4s}(pF)	16.7
C_1(pF)	89.8	C_2(pF)	89.7
C_3(pF)	8.3	C_4(pF)	8.4
C_{M1}(pF)	79.6	C_{M2}(pF)	8.4
C_{M3}(pF)	8.3		

TABLE III
PARAMETERS OF THE PROPOSED BCPT SYSTEM

Parameter	Value
V_d(V), V_o(V)	100, 100
f_s(MHz)	1
L_{p1}(μH), L_{r1}(μH)	24, 23.9
L_{p2}(μH), L_{r2}(μH)	150, 151.2
C_{p1}(nF), C_{r1}(nF)	1.22, 1.23
C_{p2}(pF), C_{r2}(pF)	115.5, 114

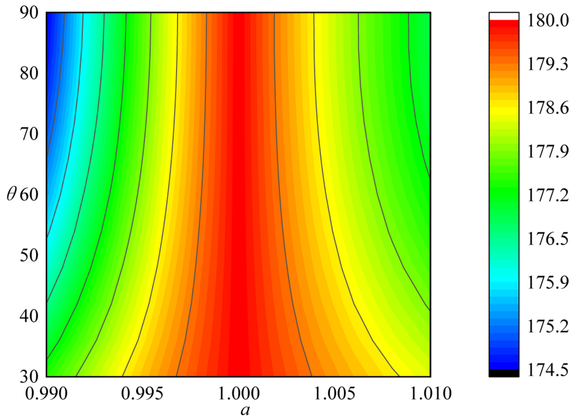

Fig. 20. Variation of the synchronous phase angle γ with the deviation resonance frequency under different relative phase-shift angles.

is 1.67% and $\gamma = 177°$; while $\theta = 30°$, the deviation of the phase angle is only 0.89% and $\gamma = 178.4°$.

In addition, due to the proposed synchronization control method, the primary (secondary) controller drives the primary (secondary) converter with the operating frequency initially, and the secondary (primary) controller obtains the frequency and phase by sampling the terminal voltage of the secondary (primary) supplementary plates, which is synchronized with the resonant voltage generated by the primary(secondary) converter to drive the secondary (primary) converter regardless of the deviation of the resonance conditions. So, the frequencies of the primary and secondary sides are synchronized regardless of the deviation of the resonance conditions.

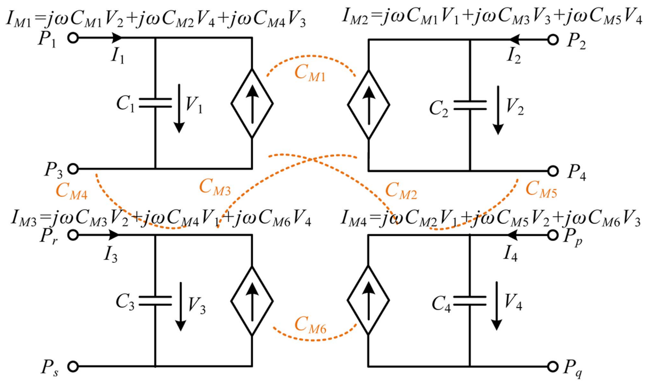

Fig. 21. Four-port circuit-source model of an eight-plate coupler.

Therefore, through the above analysis, the frequencies of the primary and secondary sides are synchronized regardless of the deviation of the resonance conditions, while the synchronous phase angle γ will be changed slightly because of the deviation of the resonant frequency. However, the deviation of the phase angle can be corrected by phase compensation.

VI. CONCLUSION

This article proposes a synchronous control method without wireless communication for phase-shift power flow regulation of the dual *LCLC*-compensated BCPT systems. The method utilizes two pairs of supplementary plates that form the composite plates coupler; the voltage of the primary (secondary) main plates is obtained by detecting the voltage of the secondary (primary) supplementary plates so as to obtain the synchronous information of the primary(secondary) converter and feed it back to the secondary(primary) controller. The main contribution of the proposed synchronous control method can be concluded as follows.

1) The proposed system realizes frequency and phase synchronization between primary and secondary sides without communication modules to facilitate the power flow regulation.
2) Due to the limitation of synchronous control by detecting currents that may have harmonics, the proposed system obtains the synchronization status by detecting the voltage of the supplementary plates and also achieves interoperability between the primary and secondary sides.
3) The proposed synchronous control method does not require PLL, VCO, complex analog circuits, and data processing analyses, which is favorable to operate at high-frequency BCPT systems.

APPENDIX

Through the analysis in Section III, the coupling capacitance model, as shown in Fig. 7, is simplified to a four-port equivalent circuit-source model, as shown in Fig. 21. The plates P_1 and P_3 are connected to the primary circuit and form the first port, the plates P_2 and P_4 are connected to the secondary circuit and form the second port, the plates P_r and P_s form the third port, and the

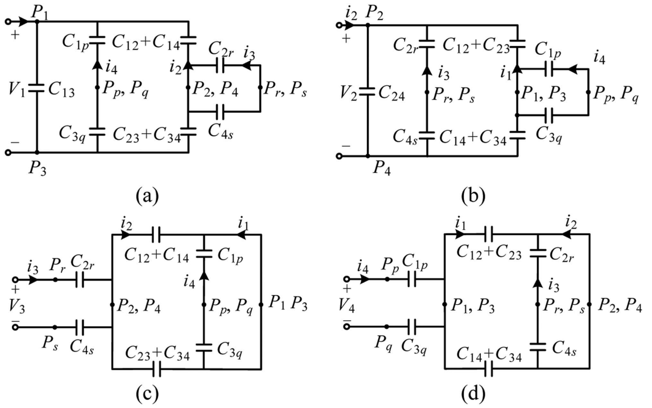

Fig. 22. Simplified capacitor model. (a) $V_2 = V_3 = V_4 = 0$. (b) $V_1 = V_3 = V_4 = 0$. (c) $V_1 = V_2 = V_4 = 0$. (d) $V_1 = V_2 = V_3 = 0$.

plates P_p and P_q form the fourth port. C_1, C_2, C_3, and C_4 are the self-capacitances of four ports, respectively. The terminal voltage and current of the four ports are expressed as V_1, I_1, V_2, I_2, V_3, I_3, V_4, and I_4. The relationship between the circuit variables is shown as follows:

$$\begin{cases} I_1 = j\omega C_1 V_1 - j\omega C_{M1} V_2 - j\omega C_{M2} V_4 - j\omega C_{M4} V_3 \\ I_2 = j\omega C_2 V_2 - j\omega C_{M1} V_1 - j\omega C_{M3} V_3 - j\omega C_{M5} V_4 \\ I_3 = j\omega C_3 V_3 - j\omega C_{M3} V_2 - j\omega C_{M4} V_1 - j\omega C_{M6} V_4 \\ I_4 = j\omega C_4 V_4 - j\omega C_{M2} V_1 - j\omega C_{M5} V_2 - j\omega C_{M6} V_3 \end{cases} \tag{16}$$

where C_{M1}, C_{M2}, C_{M3}, C_{M4}, C_{M5}, and C_{M6} are the mutual capacitances.

From (16), when V_2, V_3, and V_4 are short circuited, C_1, C_{M1}, C_{M2}, and C_{M4} can be obtained. When V_1, V_3, and V_4 are short circuited, C_2, C_{M3}, and C_{M5} can be obtained. When V_1, V_2, and V_4 are short circuited, C_3 and C_{M6} can be obtained. When V_1, V_2, and V_3 are short circuited, C_4 can be obtained. The simplified capacitor model in the above four cases is shown in Fig. 22.

Thus, C_1, C_2, C_3, and C_4 are expressed as

$$\begin{aligned} C_1 &= \left.\frac{I_1}{j\omega V_1}\right|_{V_2=V_3=V_4=0} \\ &= C_{13} + \frac{(C_{12}+C_{14})(C_{23}+C_{34})}{C_{12}+C_{14}+C_{23}+C_{34}} + \frac{C_{1p}C_{3q}}{C_{1p}+C_{3q}} \\ C_2 &= \left.\frac{I_2}{j\omega V_2}\right|_{V_1=V_3=V_4=0} \\ &= C_{24} + \frac{(C_{12}+C_{23})(C_{14}+C_{34})}{C_{12}+C_{14}+C_{23}+C_{34}} + \frac{C_{2r}C_{4s}}{C_{2r}+C_{4s}} \\ C_3 &= \left.\frac{I_3}{j\omega V_3}\right|_{V_1=V_2=V_4=0} = \frac{C_{2r}\cdot C_{4s}}{C_{2r}+C_{4s}} \\ C_4 &= \left.\frac{I_4}{j\omega V_4}\right|_{V_1=V_2=V_3=0} = \frac{C_{1p}\cdot C_{3q}}{C_{1p}+C_{3q}}. \end{aligned} \tag{17}$$

From Fig. 22(a), when V_2, V_3, and V_4 are short circuited, I_2, I_3, and I_4 represent the currents induced by V_1 and can be derived as

$$\begin{aligned} I_2|_{V_2=V_3=V_4=0} &= -j\omega\frac{(C_{12}+C_{14})(C_{23}+C_{34})}{C_{12}+C_{14}+C_{23}+C_{34}}V_1 \\ I_3|_{V_2=V_3=V_4=0} &= 0 \\ I_4|_{V_2=V_3=V_4=0} &= -j\omega\frac{C_{1p}C_{3q}}{C_{1p}+C_{3q}}V_1. \end{aligned} \tag{18}$$

Then, the mutual capacitances C_{M1}, C_{M2}, and C_{M4} can be given as follows:

$$\begin{aligned} C_{M1} &= -\left.\frac{I_2}{j\omega V_1}\right|_{V_2=V_3=V_4=0} = \frac{(C_{12}+C_{14})(C_{23}+C_{34})}{C_{12}+C_{14}+C_{23}+C_{34}} \\ C_{M2} &= -\left.\frac{I_4}{j\omega V_1}\right|_{V_2=V_3=V_4=0} = \frac{C_{1p}C_{3q}}{C_{1p}+C_{3q}} \\ C_{M4} &= -\left.\frac{I_3}{j\omega V_1}\right|_{V_2=V_3=V_4=0} = 0. \end{aligned} \tag{19}$$

When V_1 and V_3 are short circuited, I_3 can be obtained as follows:

$$I_3|_{V_1=V_3=V_4=0} = -j\omega\frac{C_{2r}C_{4s}}{C_{2r}+C_{4s}}V_2. \tag{20}$$

So, the mutual capacitances C_{M3} and C_{M5} can be derived as

$$\begin{aligned} C_{M3} &= -\left.\frac{I_3}{j\omega V_2}\right|_{V_1=V_3=V_4=0} = \frac{C_{2r}C_{4s}}{C_{2r}+C_{4s}} \\ C_{M5} &= -\left.\frac{I_4}{j\omega V_2}\right|_{V_1=V_3=V_4=0} = 0. \end{aligned} \tag{21}$$

According to Fig. 22(c), the mutual capacitance C_{M6} can be given as

$$C_{M6} = -\left.\frac{I_4}{j\omega V_3}\right|_{V_1=V_2=V_4=0} = 0. \tag{22}$$

When the eight-plate coupler is connected to the circuit, only the coupling plates P_1, P_2, P_3, and P_4 are directly connected, and the supplementary plates P_p, P_q, P_r, and P_s are externally connected to the detection circuit. It means that there is no external voltage or current source connected to P_p, P_q, P_r, and P_s, so $I_3 = I_4 = 0$. Then, (16) can be equivalent to

$$\begin{cases} I_1 = j\omega\left(C_1 - \frac{C_{M2}^2}{C_4}\right)V_1 - j\omega C_{M1}V_2 \\ I_2 = j\omega\left(C_2 - \frac{C_{M3}^2}{C_3}\right)V_2 - j\omega C_{M1}V_1. \end{cases} \tag{23}$$

Supposing

$$\begin{aligned} C_{t1} &= C_1 - \frac{C_{M2}^2}{C_4} + C_{p2} = C_{13} + \frac{(C_{12}+C_{14})(C_{23}+C_{34})}{C_{12}+C_{14}+C_{23}+C_{34}} + C_{p2} \\ C_{t2} &= C_2 - \frac{C_{M3}^2}{C_3} + C_{r2} = C_{24} + \frac{(C_{12}+C_{23})(C_{14}+C_{34})}{C_{12}+C_{14}+C_{23}+C_{34}} + C_{r2}. \end{aligned} \tag{24}$$

Therefore, combined with the *LCLC*-compensated topology diagram in Fig. 2, the four-port equivalent circuit diagram with the eight-plate coupler can be shown in Fig. 8.

According to Fig. 8, similar to (3), the resonance relationship is satisfied as follows:

$$\begin{cases}\omega_s^2 L_{p2}\left(C_{p1}\cdot C_{t1}/(C_{p1}+C_{t1})\right)=1\\ \omega_s^2 C_{p1}\left(L_{p1}\cdot L_{p2}/(L_{p1}+L_{p2})\right)=1\\ \omega_s^2 L_{r2}\left(C_{r1}\cdot C_{t2}/(C_{r1}+C_{t2})\right)=1\\ \omega_s^2 C_{r1}\left(L_{r1}\cdot L_{r2}/(L_{r1}+L_{r2})\right)=1.\end{cases} \quad (25)$$

According to the KVLs law, the relationship between the currents and voltages of the proposed BCPT system can be derived as

$$\begin{cases}V_p=j\omega L_{p1}I_p+V_{p1}\\ I_p=j\omega C_{p1}V_{p1}+I_1\\ V_{p1}=j\omega L_{p2}I_1+V_1\\ I_1=j\omega C_{t1}V_1-j\omega C_{M1}V_2\\ I_2=j\omega C_{t2}V_2-j\omega C_{M1}V_1\\ V_2=V_{r1}-j\omega L_{r2}I_2\\ I_r=j\omega C_{r1}V_{r1}+I_2.\end{cases} \quad (26)$$

The voltages V_1 and V_2 can be expressed by

$$V_1=-\frac{L_{p2}}{L_{p1}}V_p,\quad V_2=-\frac{L_{r2}}{L_{r1}}V_r. \quad (27)$$

Thus, V_3 and V_4 can be given as

$$\begin{cases}V_3=\frac{j\omega C_{M3}}{j\omega C_3}V_2=-\frac{C_{M3}L_{r2}}{C_3L_{r1}}V_r=-\frac{L_{r2}}{L_{r1}}V_r\\ V_4=\frac{j\omega C_{M2}}{j\omega C_4}V_1=-\frac{C_{M2}L_{p2}}{C_4L_{p1}}V_p=-\frac{L_{p2}}{L_{p1}}V_p.\end{cases} \quad (28)$$

The transmission power of the secondary side can be derived as

$$P_r=\mathrm{Re}\left\{V_rI_r^*\right\}=\frac{8\omega C_{M1}}{\pi^2}\frac{L_{p2}L_{r2}}{L_{p1}L_{r1}}V_dV_o\sin\theta\sin\frac{\varphi_1}{2}\sin\frac{\varphi_2}{2}. \quad (29)$$

REFERENCES

[1] Q. Xiaodong and S. Yugang, "An overview of electric-filed coupling wireless power transfer technology," *Trans. China Electrotech. Soc.*, vol. 36, no. 17, pp. 3649–3663, 2021.

[2] F. Lu, H. Zhang, H. Hofmann, and C. C. Mi, "A double-sided LC-compensation circuit for loosely coupled capacitive power transfer," *IEEE Trans. Power Electron.*, vol. 33, no. 2, pp. 1633–1643, Feb. 2018.

[3] S. Yugang, X. Shiyun, Z. Yuming, Q. Xiaodong, and T. Chunsen, "Parameter optimization of electric-field coupled wireless power transfer system with complementary symmetric LCC resonant network," *Trans. China Electrotech. Soc.*, vol. 34, no. 14, pp. 2874–2883, 2019.

[4] C. Liu, A. P. Hu, B. Wang, and N.-K. C. Nair, "A capacitively coupled contactless matrix charging platform with soft switched transformer control," *IEEE Trans. Ind. Electron.*, vol. 60, no. 1, pp. 249–260, Jan. 2013.

[5] C. Liu, A. P. Hu, and N.-K. C. Nair, "Coupling study of a rotary capacitive power transfer system," in *Proc. IEEE Int. Conf. Ind. Technol.*, Churchill, VIC, Australia, 2009, pp. 1–6.

[6] R. Sezdehi et al., "A wireless power method for deeply implanted biomedical devices via capacitively coupled conductive power transfer," *IEEE Trans. Power Electron.*, vol. 36, no. 2, pp. 1870–1882, Feb. 2021.

[7] K. V. T. Piipponen, R. Sepponen, and P. Eskelinen, "A biosignal instrumentation system using capacitive coupling for power and signal isolation," *IEEE Trans. Biomed. Eng.*, vol. 54, no. 10, pp. 1822–1828, Oct. 2007.

[8] J. Dai and D. C. Ludois, "Capacitive power transfer through a conformal bumper for electric vehicle charging," *IEEE J. Emerg. Sel. Topics Power Electron.*, vol. 4, no. 3, pp. 1015–1025, Sep. 2016.

[9] J. Dai and D. C Ludois, "Wireless electric vehicle charging via capacitive power transfer through a conformal bumper," in *Proc. IEEE Appl. Power Electron. Conf. Expo.*, Charlotte, NC, USA, 2015, pp. 3307–3313.

[10] S. Weearsinghe, D. J. Thrimawithana, and U. K. Madawala, "Modeling bidirectional contactless grid interfaces with a soft DC-link," *IEEE Trans. Power Electron.*, vol. 30, no. 7, pp. 3528–3541, Jul. 2015.

[11] B. Vardani and N. R. Tummuru, "A single-stage bidirectional inductive power transfer system with closed-loop current control strategy," *IEEE Trans. Transp. Electrific.*, vol. 6, no. 3, pp. 948–957, Sep. 2020.

[12] U. K. Madawala, N. Neath, and D. J. Thrimawithana, "A power–frequency controller for bidirectional inductive power transfer systems," *IEEE Trans. Ind. Electron.*, vol. 60, no. 1, pp. 310–317, Jan. 2013.

[13] A. A. S. Mohamed, A. A. Marim, and O. A. Mohammed, "Magnetic design considerations of bidirectional inductive wireless power transfer system for EV applications," *IEEE Trans. Magn.*, vol. 53, no. 6, Jun. 2017, Art. no. 8700105.

[14] A. K. Swain, S. Devarakonda, and U. K. Madawala, "Modeling, sensitivity analysis, and controller synthesis of multipickup bidirectional inductive power transfer systems," *IEEE Trans. Ind. Inform.*, vol. 10, no. 2, pp. 1372–1380, May 2014.

[15] D. J. Thrimawithana and U. Madawala, "A generalized steady-state model for bidirectional WPT systems," *IEEE Trans. Power Electron.*, vol. 28, no. 10, pp. 4681–4689, Oct. 2013.

[16] A. K. Swain, M. J. Neath, U. K. Madawala, and D. J. Thrimawithana, "Dynamic multivariable state-space model for bidirectional inductive power transfer systems," *IEEE Trans. Power Electron.*, vol. 27, no. 11, pp. 4772–4780, Nov. 2012.

[17] X. Dai, M. Sun, P. Deng, R. Wang, and Y. Su, "Asymmetric bidirectional capacitive power transfer method with push–pull full-bridge hybrid topology," *IEEE Trans. Power Electron.*, vol. 37, no. 11, pp. 13902–13913, Nov. 2022.

[18] U. K. Madawala and D. J. Thrimawithana, "A bidirectional inductive power interface for electric vehicles in V2G systems," *IEEE Trans. Ind. Electron.*, vol. 58, no. 10, pp. 4789–4796, Oct. 2011.

[19] B. X. Nguyen et al., "An efficiency optimization scheme for bidirectional inductive power transfer systems," *IEEE Trans. Power Electron.*, vol. 30, no. 11, pp. 6310–6319, Nov. 2015.

[20] T. Tan, K. Chen, Y. Jiang, Q. Lin, L. Yuan, and Z. Zhao, "A bidirectional wireless power transfer system control strategy independent of real-time wireless communication," *IEEE Trans. Ind. Appl.*, vol. 56, no. 2, pp. 1587–1598, Mar./Apr. 2020.

[21] L. Wang, U. K. Madawala, J. Zhang, and M.-C. Wong, "A new bidirectional wireless power transfer topology," *IEEE Trans. Ind. Appl.*, vol. 58, no. 1, pp. 1146–1156, Jan./Feb. 2022.

[22] L. Zhao, D. J. Thrimawithana, and U. K. Madawala, "Hybrid bidirectional wireless EV charging system tolerant to pad misalignment," *IEEE Trans. Ind. Electron.*, vol. 64, no. 9, pp. 7079–7086, Sep. 2017.

[23] "Bluetooth core specification version 5.0," Bluetooth Special Int. Group, Washington, DC, USA, Dec. 2016.

[24] Manpreet and J. Malhotra, "ZigBee technology: Current status and future scope," in *Proc. Int. Conf. Comput. Comput. Sci.*, Greater Noida, India, 2015, pp. 163–169.

[25] *IEEE Standard for Information Technology-Telecommunications and Information Exchange Between Systems Local and Metropolitan Area Networks—Specific Requirements—Part 11: Wireless LAN Medium Access Control (MAC) and Physical Layer (PHY) Specifications*, IEEE Standard 802.11-2016, 2016.

[26] F. Liu, K. Li, K. Chen, and Z. Zhao, "A phase synchronization technique based on perturbation and observation for bidirectional wireless power transfer system," *IEEE J. Emerg. Sel. Topics Power Electron.*, vol. 8, no. 2, pp. 1287–1297, Jun. 2020.

[27] S. Jia, C. Chen, P. Liu, and S. Duan, "A digital phase synchronization method for bidirectional inductive power transfer," *IEEE Trans. Ind. Electron.*, vol. 67, no. 8, pp. 6450–6460, Aug. 2020.

[28] D. Zhang, M. Chen, B. Li, X. Wang, X. Sun, and F. Jiang, "Synchronization strategy based on resonant current detection for bidirectional wireless charging system," *IEEE Trans. Power Electron.*, vol. 37, no. 9, pp. 11436–11449, Sep. 2022.

[29] Y. Tang, Y. Chen, U. K. Madawala, D. J. Thrimawithana, and H. Ma, "A new controller for bidirectional wireless power transfer systems," *IEEE Trans. Power Electron.*, vol. 33, no. 10, pp. 9076–9087, Oct. 2018.

[30] D. J. Thrimawithana, U. K. Madawala, and M. Neath, "A synchronization technique for bidirectional WPT systems," *IEEE Trans. Ind. Electron.*, vol. 60, no. 1, pp. 310–317, Jan. 2013.

[31] F. Lu, H. Zhang, H. Hofmann, and C. Mi, "A double-sided LCLC-compensated capacitive power transfer system for electric vehicle charging," *IEEE Trans. Power Electron.*, vol. 30, no. 11, pp. 6011–6014, Nov. 2015.

[32] P. J. Vishnu and N. R. Tummuru, “A phase shift control strategy for bidirectional power flow in capacitive wireless power transfer system using LCLC compensation,” in *Proc. IEEE Int. Conf. Power Electron., Smart Grid Renewable Energy*, 2020, pp. 1–6.

Min Sun (Graduate Student Member, IEEE) received the B.E. degree in automation from the College of Artificial Intelligence, Chongqing Technology and Business University, Chongqing, China, in 2017. She is currently working toward the Ph.D. degree in control theory and control engineering with Chongqing University, Chongqing, China.

Her current research interests include the bidirectional wireless power transfer and power electronics.

Xin Dai (Member, IEEE) received the B.S. degree in industrial automation from Yuzhou University, Chongqing, China, in 2000, and the Ph.D. degree in control theory and control engineering from the School of Automation, Chongqing University, Chongqing, China, in 2006.

In 2012, he was a Visiting Scholar with The University of Auckland, Auckland, New Zealand. He is currently a Professor with the School of Automation, Chongqing University. His research interests include inductive power transfer technology and nonlinear dynamic behavior analysis of power electronics.

Yugang Su (Member, IEEE) received the B.E. and M.E. degrees in industry automation and the Ph.D. degree in control theory and control engineering from Chongqing University, Chongqing, China, in 1985, 1993, and 2004, respectively.

From 2008 to 2009, he was a Visiting Scholar with the University of Queensland, Brisbane, Australia. He is currently a Professor with the College of Automation, Chongqing University. His research interests include power electronics, control theory and applications, and wireless power transfer.

Yanling Li received the Ph.D. degree from the School of Automation, Chongqing University, Chongqing, China, in 2017.

She is currently working with the School of Electrical Engineering and Electronics Information, Xihua University, Chengdu, China. Her research interests include wireless power transfer and advanced control technology in power electronics.

Shijun Zhao (Graduate Student Member, IEEE) was born in Sichuan, China. He received the B.Eng. degree in automation from the Faculty of Information Engineering and Automation, Kunming University of Science and Technology, Kunming, China, in 2017. He is currently working toward the Ph.D. degree in control theory and control engineering with Chongqing University, Chongqing, China.

His current research interests include modeling, system identification, and control methods of wireless power transfer and power electronics.